

Chiral Edge Current in Nematic Cell Monolayers

V. Yashunsky^{1,*}, D. J. G. Pearce^{2,3,4,†}, C. Blanch-Mercader^{2,3,†}, F. Ascione¹, P. Silberzan^{1,†} and L. Giomi^{5,†}

¹*Laboratoire Physico-Chimie Curie, Institut Curie, PSL Research University-Sorbonne Université, CNRS, 75005 Paris, France*

²*Department of Physics, University of Geneva, 1211 Geneva, Switzerland*

³*Department of Biochemistry, University of Geneva, 1211 Geneva, Switzerland*

⁴*Department of Mathematics, Massachusetts Institute of Technology, Cambridge, Massachusetts 02142, USA*

⁵*Instituut-Lorentz, Universiteit Leiden, P.O. Box 9506, 2300 RA Leiden, Netherlands*



(Received 7 May 2021; revised 13 July 2022; accepted 16 August 2022; published 14 November 2022)

Collectively migrating cells in living organisms are often guided by their local environment, including physical barriers and internal interfaces. Well-controlled *in vitro* experiments have shown that, when confined in adhesive stripes, monolayers of moderately active spindle-shaped cells self-organize at well-defined angle to the stripes' longitudinal direction and spontaneously give rise to a simple shear flow, where the average cellular orientation smoothly varies across the system. However, the impact of physical boundaries on highly active, chaotic, multicellular systems is currently unknown, despite its potential relevance. In this work, we show that human fibrosarcoma cells (HT1080) close to an interface exhibit a spontaneous edge current with broken left-right symmetry, while in the bulk the cell flow remains chaotic. These localized edge currents result from an interplay between nematic order, microscopic chirality, and topological defects. Using a combination of *in vitro* experiments, numerical simulations, and theoretical work, we demonstrate the presence of a self-organized layer of $+1/2$ defects anchored at the boundary and oriented at a well-defined angle close to, but smaller than, 90° with respect to the boundary direction. These self-organized defects act as local sources of chiral active stress generating the directed edge flows. Our work therefore highlights the impact of topology on the emergence of collective cell flows at boundaries. It also demonstrates the role of chirality in the emergence of edge flows. Since chirality and boundaries are common properties of multicellular systems, this work suggests a new possible mechanism for collective cellular flows.

DOI: [10.1103/PhysRevX.12.041017](https://doi.org/10.1103/PhysRevX.12.041017)

Subject Areas: Biological Physics, Soft Matter

I. INTRODUCTION

Whether eukaryotes or prokaryotes, the development and survival of multicellular systems, such as epithelial or endothelial tissues, bacterial colonies, and biofilms, crucially rely on the ability of cells to migrate collectively [1,2]. This functionality lies at the heart of many physiological process, such as embryonic morphogenesis [3] and wound healing [4], but also of pathological conditions, from bacterial infections [5] to metastatic cancer [6,7]. While commonly ascribed to the cell signaling machinery, it has recently

become obvious that these processes further hinge on mechanical cues acting at length scales several times larger than that of the individual cells [8,9]. Depending on the cell shape and motility, as well as the mechanical and geometrical properties of the environment, *in vitro* cell layers have been observed to display a large variety of dynamical behaviors, ranging from collective jamming to chaotic flows reminiscent of turbulence in driven fluids [10–15].

Harnessing the motility of cells in order to achieve multicellular organization and biological functionality requires a toolbox of reliable and robust control mechanisms, whose exploration and understanding are still in their infancy. In this respect, the possibility that multicellular systems could take advantage of *topological* mechanisms represents one of the most fascinating and promising hypotheses explaining the robustness of a variety of emerging multicellular dynamics.

Topological mechanisms have become an essential part of the understanding of both the classical and quantum world. In the realm of active matter, topological mechanisms are often associated to defects, namely, point or line singularities within otherwise well-ordered media. The importance of such topological defects has recently been highlighted in

*victoryashunsky@gmail.com

†These authors contributed equally to this work.

‡Department of Solar Energy and Environmental Physics, The Blaustein Institutes for Desert Research, Ben-Gurion University of the Negev, Midreshet Ben-Gurion, Negev, 84990, Israel.

§daniel.pearce@unige.ch

Published by the American Physical Society under the terms of the [Creative Commons Attribution 4.0 International](https://creativecommons.org/licenses/by/4.0/) license. Further distribution of this work must maintain attribution to the author(s) and the published article's title, journal citation, and DOI.

developmental processes in eukaryotic organisms, such as the large-scale cell rearrangements in the *Drosophila* embryo [16] and the growth of tentacles in *Hydra* [17], as well as cell apoptosis and extrusion in epithelia [18]. The ability of certain topological defects to self-propel is now an established concept in the physics of active fluids [19–21]. When activity is sufficiently large, topological defects can spontaneously nucleate [19] and their proliferation is generally associated with chaos [22,23], hence, to the *lack* of directed motion. So far, no compelling evidence has suggested that topological defects could play a role in a generic cell migration strategy for highly dynamic cellular systems that exhibit signatures of active turbulent behavior [14,24,25].

Left-right symmetry breaking (chirality) is another property that is present in a many cell types [26]. At the single cell level it is associated with the chiral organization of the actin cytoskeleton [27–29]. Interestingly, chirality is also a general property of cell assemblies [26,30–32]. The mechanism by which chirality is transferred from individual cells to multicellular groups is unclear; however, treatments that reverse the direction of actin chirality in single cells also change the direction of multicellular chirality [26,33].

In this article we show that in highly active cell monolayers topological defects can coalign at physical boundary where they trigger a directed cellular flow. Specifically, we study the mechanics of highly active spindle-shaped human fibrosarcoma cell (HT1080) monolayers within adhesive stripes. Because of their large activity and elongated shape, these cells give rise to a collective state known as “active nematic turbulence,” where the cells are locally aligned and yet chaotically moving and topological defects, such as $\pm 1/2$ disclinations, persistently unbind and annihilate. Thanks to a combination of *in vitro* experiments and hydrodynamic simulations of active matter, we show that long-ranged chiral flow arises at the boundary of the stripe. Such a flow is generated by $+1/2$ topological defects, which tend to align nearly perpendicular to the boundary and act as local sources of chiral active stress. Remarkably, this mechanism does not rely on actual confinement, as in the case of edge currents in dense bacterial suspensions [34–37] and defect-free nematic cell monolayers [32]. The edge currents reported here do not require confining walls, which explicitly break the rotational symmetry of the flow by setting the cells’ direction of motion, but rely exclusively on the presence of an interface, which serves as organizing center for $+1/2$ defects. A signature of such a difference is that HT1080 edge currents are not affected by the width of the stripes, unlike in previously reported cases [32,36,37], therefore highlighting the *topological* (i.e., nonmetric) nature of HT1080 edge currents.

II. EDGE CURRENTS IN DISORDERED FIBROSARCOMA CULTURES

We investigate collective dynamics of human fibrosarcoma cells (HT1080) cultured on adhesive stripes

surrounded by repellent coating [38] (see Movie 1 in Supplemental Material [39]). The stripe width L_x varies in the range 300–1000 μm . Although initially sparse upon the plating, the cells proliferate and eventually form a confluent monolayer without visible gaps, a process which typically takes on the order of 24 hours [Fig. 1(a)]. The spatial organization of the cellular layer is revealed by its orientational anisotropy [Fig. 1(b)], characterized in terms of the two-dimensional nematic tensor $\mathbf{Q} = S(\mathbf{nn} - \mathbb{1}/2)$. In which the unit vector \mathbf{n} is the nematic director and S is the scalar order parameter, describing the cells’ average orientation and degree of alignment, respectively ($\mathbb{1}$ is the identity tensor). \mathbf{Q} was measured from phase-contrast images with a structure tensor method (see the Appendix). We find a nonvanishing order parameter $\langle S \rangle = 0.19 \pm 0.02$ (mean \pm standard deviation for 24 stripes, within a field of view), which remains nearly constant over the measurement time (see Fig. S1 in Supplemental Material [39]). This value is larger than in the case of the Madin-Darby canine kidney (MDCK) cell monolayers, comparable to human bronchial epithelial cells (HBEC) [14] and to mouse myoblasts (C2C12) [21] at the early times of monolayer formation. When confined in stripes wider than 300 μm , HT1080 monolayers organize in multiple domains of coaligned cells separated by $\pm 1/2$ topological defects [marked in red and blue in Fig. 1(b)]. Despite the irregular dynamics of HT1080 cells (Movie 1 [39]), such a multidomain organization persists throughout experiments (>25 h), as indicated by the constant level of orientational anisotropy (Fig. S1 [39]).

Figure 1(c) shows a particle image velocimetry (PIV) reconstruction of the collective cellular flow. Unlike epithelial cell types, such as MDCK or HBEC [14], which relax toward a jammed state after reaching confluence, in HT1080 layers the root mean square speed $v_{\text{rms}} = \sqrt{\langle |\mathbf{v}|^2 \rangle}$ remains constant for over 25 h, with $v_{\text{rms}} = 12.1 \pm 0.6$ $\mu\text{m}/\text{h}$ (mean \pm standard deviation for 40 stripes; see Fig. S2 [39] of Supplemental Material). The flow is disorganized in the bulk, with regions of positive (red) and negative (blue) vorticity tiling the channel in an irregular yet homogeneous fashion [Fig. 1(c)]. Remarkably, however, averaging these irregular flows over the length of the stripe and in time (see Appendix for details) reveals a net chiral flow at the boundary [Fig. 1(d) herein and Fig. S3 of Supplemental Material [39]]. This statistical flow is localized within a boundary layer of approximate size 23 μm , independent of the channel width [Fig. 1(d), inset], and oppositely directed at the two lateral edges of the channel [Fig. 1(d)]. Despite the channel being perfectly symmetric with respect to reflections about its centerline, such an edge current is almost exclusively right-handed [Fig. 1(f) herein and Fig. S3 [39]] and stable in time (Fig. S4 [39]). Specifically, of the 360 analyzed fields of view in more than 200 stripes (see Appendix for details), the edge current is found to be right-handed in 95% of cases, whereas in the remaining 5% of cases, the system does not develop a net

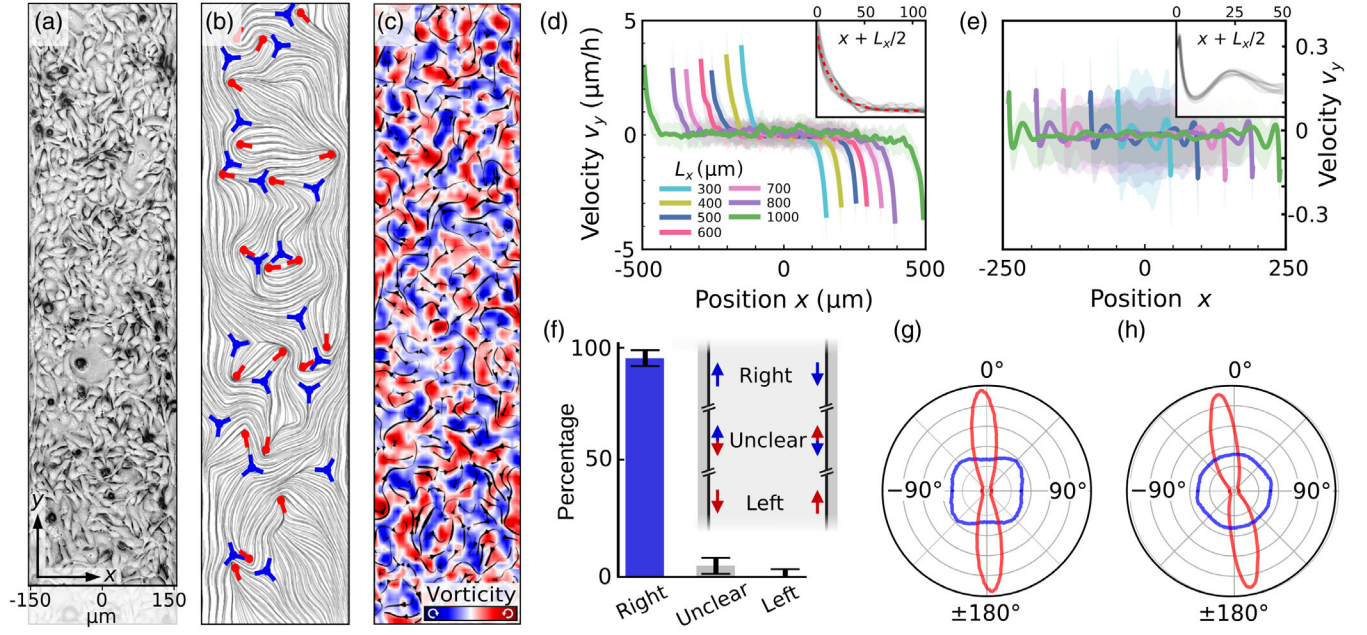


FIG. 1. HT1080 cell monolayer on an adhesive stripe. (a) Phase contrast image in inverted gray scale. (b) The nematic director field extracted from (a) with positive (red) and negative (blue) locations and orientations of half integer defects. (c) Black velocity streamlines are overlaid on the normalized vorticity field (blue, clockwise; red, counterclockwise). (d) Average flow along the channel shows boundary flows with net chirality. Boundary flows have a constant width independent of channel dimensions which can be observed by translating the curves onto each other. This exposes a constant decay length ($23 \mu\text{m}$) that can be estimated by fitting an exponential (dashed red line, $R^2 = 0.99$) (inset). (e) Average flow for a simulated chiral active nematic ($\alpha = -10$, $\tau = -2.5$) also shows boundary flows with net chirality and constant length scale (inset). (f) Chirality of edge flow direction in 360 fields of view is right-handed in 95% of cases and unclear in the remaining 5% of cases (see Appendix for details). (g) Average cell orientation at the edge (red) and center (blue) of the channel showing boundary alignment with a chiral tilt. (h) Average director orientation at the edge (red) and center (blue) for a simulated chiral active nematic, again with boundary alignment with a distinct chiral tilt. Simulation units and parameter values are given in the Appendix.

flow along the boundaries [Fig. 1(f)]. These results strongly indicate a breakdown of parity symmetry and the emergence of chirality at the length scale of the entire system.

To shed light on the emergence of these chiral edge currents, we have complemented our *in vitro* experiments with a computational model based on the hydrodynamic theory of active nematic liquid crystals [40,41]. Similar approaches have been successfully used to account for the emergent behavior of a vast class of multicellular systems, such as bacteria suspensions, [42–45] and epithelial cell monolayers [46–51].

The evolution of the nematic tensor (\mathbf{Q}) and the velocity field (\mathbf{v}) are governed by the following equations:

$$\frac{D\mathbf{Q}}{Dt} = \lambda \mathbf{S}\mathbf{u} + \mathbf{Q} \cdot \boldsymbol{\omega} - \boldsymbol{\omega} \cdot \mathbf{Q} + \gamma^{-1} \mathbf{H}, \quad (1a)$$

$$\rho \frac{D\mathbf{v}}{Dt} = \eta \nabla^2 \mathbf{v} + \nabla \cdot (-P\mathbb{1} + \boldsymbol{\sigma}) - \mu \mathbf{v}, \quad (1b)$$

where $D/Dt = \partial_t + \mathbf{v} \cdot \nabla$ is the material derivative, $\mathbf{u} = [\nabla \mathbf{v} + (\nabla \mathbf{v})^T]/2$ and $\boldsymbol{\omega} = [\nabla \mathbf{v} - (\nabla \mathbf{v})^T]/2$ are, respectively, the strain rate and vorticity tensor, λ is the flow alignment parameter, dictating how the nematic director rotates in a

shear flow, and γ is a rotational viscosity. The quantity $\mathbf{H} = -\delta F/\delta \mathbf{Q}$ is the molecular tensor driving the relaxation of the nematic tensor toward the lowest free-energy configuration. We introduce

$$F = \frac{1}{2} K \int dA \left[|\nabla \mathbf{Q}|^2 + \frac{1}{\epsilon^2} \text{tr} \mathbf{Q}^2 (\text{tr} \mathbf{Q}^2 - 1) \right], \quad (2)$$

the Landau–de Gennes free energy of the system. We assume a single elastic constant K with dimensions of energy which gives the cost of distortions in the nematic director \mathbf{Q} . The parameter ϵ is a length scale setting the typical core radius of the topological defects. In Eq. (1b), ρ is the mass density, η the shear viscosity, μ a drag coefficient resulting from the frictional interaction with the substrate, and P the hydrostatic pressure. The tensor $\boldsymbol{\sigma}$ embodies the stresses associated with the orientational degrees of freedom and can be customarily decomposed into passive and active components; i.e., $\boldsymbol{\sigma} = \boldsymbol{\sigma}^{(p)} + \boldsymbol{\sigma}^{(a)}$. The passive stress resulting from a flow-driven distortion of the nematic director is given by $\boldsymbol{\sigma}^{(p)} = -\lambda \mathbf{S}\mathbf{H} + \mathbf{Q} \cdot \mathbf{H} - \mathbf{H} \cdot \mathbf{Q}$, whereas $\boldsymbol{\sigma}^{(a)}$ accounts for the active stresses arising in the system as a consequence of the cells converting chemical fuel into mechanical work.

Now, in achiral active nematics, $\sigma^{(a)}$ results from microscopic forces generated by the active subunits along their longitudinal direction. That is, $\mathbf{F} = \pm F_{\parallel} \boldsymbol{\nu}$, where $\boldsymbol{\nu}$ is a vector describing the orientation of individual subunits. At the mesoscopic scale, and in the absence of microscopic chirality, these give rise to an active stress of the form $\sigma^{(a)} = \alpha \mathbf{Q}$. The phenomenological constant α reflects the biomechanical activity of individual subunits and is given by $\alpha = 2a\rho F_{\parallel}$, with a the cell length and ρ the number density [52,53]. In the presence of an intrinsic chirality at the cellular scale, which presumably results from the swirling of the cytoplasmic actin [27,54], microscopic forces are augmented with a transverse component; i.e., $\mathbf{F} = \pm(F_{\parallel} \boldsymbol{\nu} + F_{\perp} \boldsymbol{\nu}^{\perp})$, with $\boldsymbol{\nu} \cdot \boldsymbol{\nu}^{\perp} = 0$. This gives rise to an active stress of the form

$$\sigma^{(a)} = \alpha \mathbf{Q} - 2\tau \boldsymbol{\varepsilon} \cdot \mathbf{Q}, \quad (3)$$

where $\tau = a\rho F_{\perp}$ and $\boldsymbol{\varepsilon}$ is the antisymmetric Levi-Civita tensor [55]. With Eq. (3) in hand, we have numerically integrated Eqs. (1) of a chiral active nematic in a two-dimensional $L_x \times L_y$ rectangular domain with periodic boundary conditions at $y = \pm L_y/2$ and stress-free boundary conditions at $x = \pm L_x/2$ (see Appendix for details). Figure 1(e) shows the computed average longitudinal component of the velocity field $\langle v_y \rangle$ as a function of the distance x from the channel centerline. Consistent with our experimental observations [Fig. 1(d)], the flow is chaotic in the bulk with vanishing time-averaged velocity, but characterized by chiral edge currents, penetrating inside the bulk by an amount independent of the channel width [Fig. 1(e), inset]. Analogously, in both our *in vitro* and *in silico* cell layers, the nematic director is randomly oriented in the bulk of the channel and almost parallel to the lateral edges at the boundary [Figs. 1(g) and 1(h)].

III. TOPOLOGICAL ORIGIN OF EDGE CURRENTS

In the following we demonstrate that the edge currents observed in our experiments and simulations have a topological origin, which can be ascribed to the concerted action of $+1/2$ disclinations that spontaneously orient orthogonally to the channel walls, and the hydrodynamic flow resulting from the chiral active stresses. In nematic cell monolayers, disclinations are pointlike singularities where the orientation of the cells is undefined and around which the nematic director \mathbf{n} rotates by $2\pi s$, with $s = \pm 1/2, \pm 1, \dots$ the *winding number*. Unlike passive nematics, where topological defects annihilate under the effect of their elastic interactions, two-dimensional active nematics can feature a steady density of $\pm 1/2$ disclinations resulting from the instability of the nematic director under the flow generated by the active stress [23]. Although originating from the active flow, $\pm 1/2$ disclinations leave a distinct signature on the flow itself, whose local structure is

almost entirely determined by the configuration of the nematic director around the defect core, via the so-called *backflow* mechanism [19,20]. In particular, $+1/2$ disclinations in achiral active nematics drive a Stokeslet-like local flow consisting of two vortices symmetrically counterrotating about the defect longitudinal direction, $\mathbf{p} = \nabla \cdot \mathbf{Q} / |\nabla \cdot \mathbf{Q}|$ [56] [Fig. 2(e)]. This characteristic flow pattern causes a local flow at the center of the defect parallel with its orientation \mathbf{p} causing $+1/2$ defects to self-propel. In the present situation, cometlike defects move head first, which corresponds to an extensile nematic [Fig. 2(c)].

Chirality affects the flow around a $+1/2$ defect by tilting its mirror-symmetry axis with respect to \mathbf{p} by an angle

$$\theta_{\text{tilt}} = \arctan\left(\frac{2\tau}{\alpha}\right), \quad (4)$$

with α and τ the active stresses appearing in Eq. (3) [55] [Fig. 2(e)]. The latter property can be understood by noticing that the active part of the stress tensor can be expressed as $\sigma^{(a)} = \sqrt{\alpha^2 + 4\tau^2} \mathbf{R} \cdot \mathbf{Q} \cdot \mathbf{R}^T$, where \mathbf{R} represents a counterclockwise rotation by an angle $\theta_{\text{tilt}}/2$ and T denotes transposition.

When we analyzed the average flows in the vicinity of $+1/2$ defects in HT1080 monolayers in boundary-free cell cultures, the average flow field revealed a vortex-pair flow pattern [Fig. 2(c); see the Appendix for details]. This confirms that the active stress is extensile, $\alpha < 0$, with an average speed of $0.67 \pm 0.05 \mu\text{m/h}$ at the defect core (mean \pm standard deviation for 56 729 defects). This average flow at the core of the defect is significantly tilted relative to the orientation of the defect by $3.4^\circ \pm 0.3$ (mean \pm standard deviation for 143 185 defects) indicating a stress chirality of the order of $\tau/\alpha = 0.03$. This is very close to the theoretically predicted flow field around a $+1/2$ defect with the same stress chirality [Fig. 2(e)]. When the average flow field was computed for an equal-sized set of random points in boundary-free cell cultures, the vortex-pair pattern was lost (Fig. S5 [39]) and the average speed decreased to $0.03 \pm 0.01 \mu\text{m/h}$ (mean \pm standard deviation for 56 729 defects).

When the director field orients tangentially at the boundary, we expect some degree of local defect ordering. This is because the nematic configuration around a $+1/2$ defect that minimizes the elastic energy, Eq. (2), is such that $\mathbf{p} = -\mathbf{N}$, with \mathbf{N} the stripe's outer unit normal. In extensile active nematics, $+1/2$ defects self-propel in the $-\mathbf{p}$ direction, causing them to stall close to the boundary. The chiral stresses, embodied in the constant τ in Eq. (3), explicitly break the mirror symmetry of the vortex pair around a $+1/2$ defect, tilting the flow field with respect to the defect orientation \mathbf{p} . The chiral tilt when $\tau < 0$ pushes the right-handed (or left-handed for $\tau < 0$) vortex of each pair closer to the boundary. This effect is confirmed by analyzing the flow around $+1/2$ defects located close to

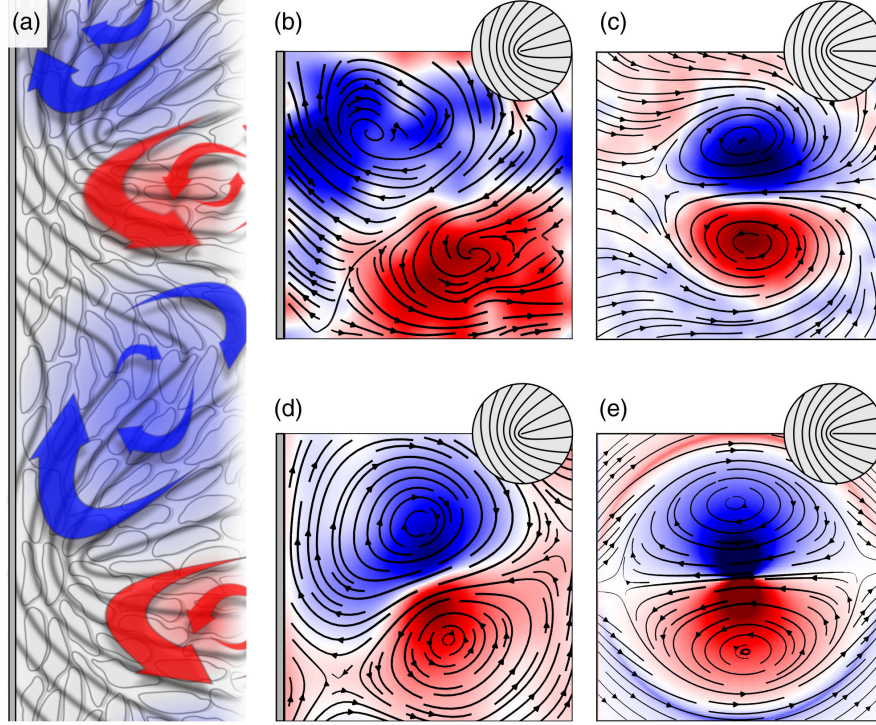


FIG. 2. (a) Schematic of the hypothesized behavior of defects close to the boundary. Motion of $+1/2$ defects and elastic interactions lead to an accumulation of defects aligned quasiperpendicular to the left boundary. The chiral activity leads to a net flow along the boundary. (b) Average flow around $56\,729 + 1/2$ defects in a HT1080 monolayer close to the boundary (gray line) with a chiral tilt of 32.5° relative to the defect orientation (inset). (c) Average flow around $143\,185 + 1/2$ defects in a HT1080 monolayer far from the boundary with a chiral tilt of 3.4° relative to the defect orientation (inset). (d) Average flow around $+1/2$ defects made over 10^6 time steps in a simulated chiral active nematic ($\alpha = -10.0$, $\tau = -1.25$) close to the left boundary (gray line). This shows a tilt relative to the average defect orientation (inset). (e) Stokeslet-like flow around an isolated chiral active $+1/2$ defect recreating tilt of 3.4° ($\tau = 0.03\alpha$) relative to the defect orientation (inset). Dimensions in (b) and (c) correspond to $250 \times 250 \mu\text{m}^2$.

the boundary. In both simulations and experiments, the average flow pattern around a $+1/2$ defect exhibited a vortex pair that was tilted with respect to the boundary normal [Figs. 2(b) and 2(d)]. The net effect of this organization is a boundary layer of net vorticity, resulting in the detectable chiral shear flow [Figs. 1(d) and 1(e)]. Moreover, as a shear flow rotates the nematic director, such an effect results in a slight, but visible, tilt of the defect \mathbf{p} toward the flow, thus further reinforcing the chiral edge current [Fig. 2(a)].

IV. STRUCTURE AND DYNAMICS OF CHIRAL EDGES

In order to further test the proposed mechanism, we compared space-dependent defect properties in both simulations and experiments (Fig. 3). To this end, we quantify the local $+1/2$ defect density as $\rho_+(x) = N_+(x)/(\Delta x L_y)$, where $N_+(x)$ is the number of $+1/2$ defects in a thin stripe of width Δx centered at position x and running the length of the channel L_y . This is given by $N_+(x) = \sum_i \int_{x-\Delta x/2}^{x+\Delta x/2} dx' \int_{-L_y/2}^{L_y/2} dy' \delta(\mathbf{r}' - \mathbf{r}_i)$, with the summation extended over all $+1/2$ defects in

the system at positions \mathbf{r}_i . Similarly, the local $+1/2$ defect polarization can be quantified: $\mathbf{P}_+(x) = 1/N_+(x) \sum_i \int_{x-\Delta x/2}^{x+\Delta x/2} dx' \int_{-L_y/2}^{L_y/2} dy' \mathbf{p}_i \delta(\mathbf{r}' - \mathbf{r}_i)$. The system features a steady and spatially uniform distribution of the $+1/2$ disclinations away from the boundaries [Figs. 3(a) and 3(b)]. In the interior of the channel, these have no preferential orientation, as marked by the fact that the average amplitude of the polarization $P_+ = |\mathbf{P}_+|$ and the nematic order parameter vanishes [Figs. 3(c) and 3(d) herein and Fig. S6 in Supplemental Material [39]]. By contrast, P_+ and the nematic order parameter have a maximum close to the boundaries, indicating the existence of a persistent layer of coaligned $+1/2$ defects [Figs. 3(c) and 3(d) herein and Fig. S6 [39]]. Figures 3(e) and 3(f) show the polar histograms of the $+1/2$ defect direction \mathbf{p} in the bulk and near the boundaries of the channel. Whereas there is no alignment in the bulk, at the boundaries we found an average tilt of the defects of $16 \pm 34^\circ$ (mean \pm standard deviation for 56729 defects) at the boundary for HT1080 cell monolayers [Fig. 3(e)]. This confirms the aforementioned orthogonally organized boundary layer of $+1/2$ defects with a chiral tilt that is independent of the channel geometry.

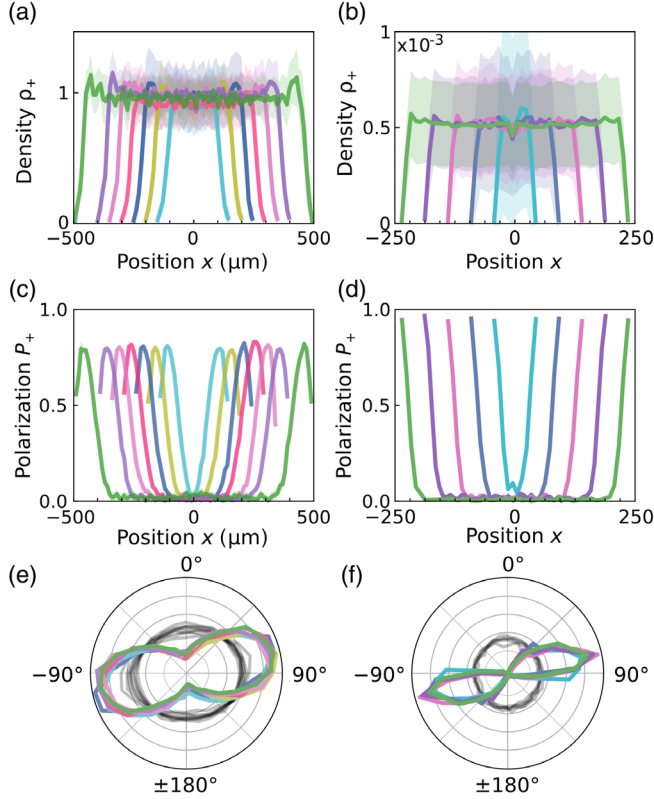


FIG. 3. (a),(b) Density of +1/2 defects in (a) monolayers of HT1080 cells in stripes normalized by the density at the center of the stripe and (b) simulated chiral active nematics ($\alpha = -10$, $\tau = -2.5$). For HT1080 monolayers, defect density is normalized to 1 in the bulk. (c),(d) Polar order parameter of +1/2 defects in (c) monolayers of HT1080 cells and (d) simulated chiral active nematics, showing orientational ordering of defects close to the boundary. (e),(f) Polar histogram of defect orientation close to the boundaries for (e) monolayers of HT1080 cells and (f) simulated chiral active nematics. The defects are on average aligned perpendicular to the boundary with a chiral tilt. In the bulk there is no net alignment (gray). Color code indicates the width of the stripe as in Fig. 1. Simulation units and parameter values are given in the Appendix.

Using numerical simulations we can further explore the effect of the chiral active stress τ on the performance of the edge current. As shown in Fig. 4, both the speed v_y of the edge current [Fig. 4(a) herein and Fig. S7(a) [39]] and the density of +1/2 defects [Fig. 4(b)] increase with τ . The latter, in particular, implies a reduction of the inter-defect spacing, which, in turn, causes the chiral boundary layer to become narrower and sharper (Fig. S7 [39]). This results in a higher local shear rate, which further accentuates the rotation of the nematic director Fig. 4(c), hence the tilt of the defect layer Fig. 4(d).

Finally, Fig. 5 shows the penetration depth ℓ as a function of the active stresses α and τ , obtained from numerical simulations for different values of the defect core radius ϵ . We estimate ℓ as the position of the first minimum of v_y [see insets in Fig. 1(e) herein and Fig. S7(a) [39]], after which the

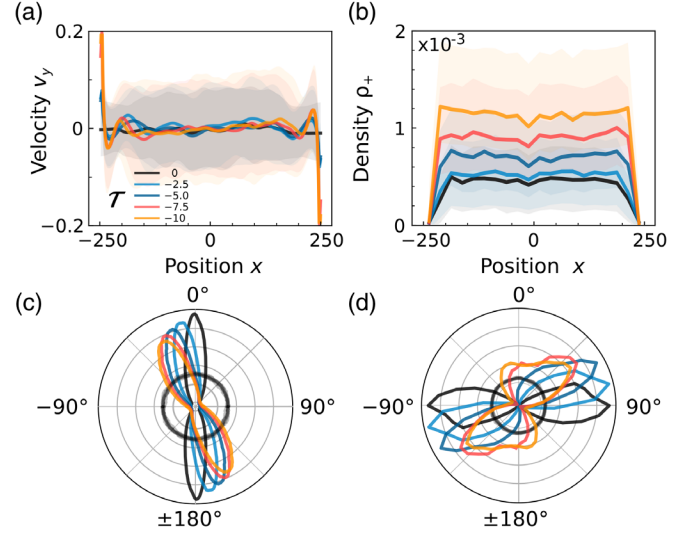


FIG. 4. (a) Average flow for simulated chiral active nematics. The net chiral flow increases in magnitude for increased chiral stress; see Fig. S7 for a close-up [39]. (b) The defect density increases with increased chiral stress. (c) The average tilt of the director close to the boundary increases with increased chiral stress. (d) Average +1/2 defect orientation close to the boundary. The magnitude of the chiral tilt increases with the chiral stress. Simulation units and parameter values are given in the Appendix.

mean velocity vanishes. These data indicate that ℓ is essentially independent of the active stress α [Fig. 5(a)], but does become shorter and shorter as the chiral stress τ is increased in magnitude [Fig. 5(b)]. This behavior originates from the mirror symmetry of the backflow sourced by +1/2 defects. For small or vanishing τ values, defects are orthogonal to the boundaries and the net edge flow resulting from them, consisting of an array of vortices with alternating positive and negative vorticity (i.e., $\omega_{\text{vortex}} \approx \pm\alpha/\eta$), has nearly vanishing speed. In this case increasing α increases ω_{vortex} , but without changing the structure of the vortex array, hence the speed of the net edge flow. Conversely, increasing τ has the effect of increasing θ_{tilt} , thereby enhancing the directionality of the edge flow and increasing

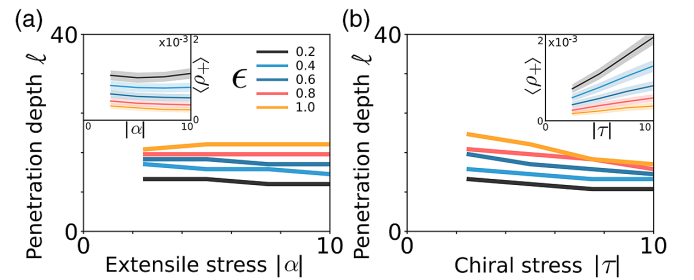


FIG. 5. Penetration depth ℓ of the chiral edge currents versus magnitude of active stresses. (a) Extensile stress α ($\tau = -5$) and (b) chiral stress τ ($\alpha = -10$). Insets: the average density $\langle\rho_+\rangle$ of +1/2 defects versus the active stresses.

its speed. The latter drives an increase of the shear stress near the boundary, which, in turn, drives a further distortion of the nematic direction that can be mitigated by the unbinding of additional defects (insets of Fig. 5). As the density of defects increases, their distance to the boundary becomes smaller, leading to the shortening of the penetration depth ℓ shown in Fig. 5(b). Lastly, enlarging the defect core radius, whose radius ϵ is proportional to the nematic coherence length, has the predictable effect of increasing the distance of the vortices to the boundary, hence the penetration depth.

V. CONCLUSIONS

In conclusion, in the presence of a boundary, HT1080 monolayers organize into a novel collective state, characterized by the existence of chiral edge currents. Compared to healthy fibroblast cell monolayers, malignant fibroblast HT1080 monolayers do not slow down with time and organize in smaller nematic domains [57]. Such a difference could be attributed to the fact that fibroblast migration strongly relies on adhesion to the substrate, and thus is affected by deposition of the extracellular matrix, whereas HT1080 (similar to other highly invasive cancer cells) display weaker adhesion to the substrate and their migration is less dependent on focal adhesions [58]. Together, these properties lead to a highly chaotic dynamics known as active turbulence and associated with the proliferation of topological defects. Far from the boundaries, the cells exhibit disordered chaotic flows, with no net motion. The cellular flow is, however, rectified along the edges, leading to long-ranged collective cell migration, with net chirality.

Modeling the system as a chiral active nematic liquid crystal, we demonstrated that, consistent with experimental observations on stripes of various width, peripheral $+1/2$ topological defects tend to align orthogonally with respect to the boundary. By contrast, even a very small chiral active stress ($\sim 3\%$ of the total active stress in the case of HT1080 cell monolayer) deviates the anchoring angle of $+1/2$ defects. This tilt of $+1/2$ defects, as well as of the vortex pairs coupled to them, is sufficient to result in global symmetry breaking and emergence of the chiral edge flows via this new mechanism, where $+1/2$ defects act as local sources of chiral active stress.

Other examples of edge currents in active living matter have been reported in particular in bacterial suspensions [34,36,37] and in ordered spindle-shaped cell cultures [32,59]. However, in all these examples, edge currents rely on confinement geometry (a stripe or a droplet). The situation is different here, since in the present case a single boundary in an otherwise unlimited system guarantees the existence of directed edge currents, even when the cellular flow is chaotic in the bulk. We emphasize here that, as unveiled by our model, chirality is indispensable to tilt the vortices originating from the defects with respect to the defects' own direction, thus to convert the alignment of $+1/2$ defects into edge currents.

Topological mechanisms have recently been evidenced as key in several morphogenic processes [2,17,60,61]. We show here that they can also be at the origin of dynamic phenomena such as collective migration. Finally, our findings establish a physical basis for a novel mechanism of chirality-induced topological edge modes in out-of-equilibrium nematic systems.

Images, videos, and numerical simulation data are available from the authors upon request.

ACKNOWLEDGMENTS

It is a pleasure to thank the members of the Biology-inspired Physics at MesoScales (BiPMS) group. The BiPMS team is member of the Cell(n)Scales Labex (Grants No. ANR-11-LABX-0038 and No. ANR-10-IDEX-0001-02) and is associated to the IPGG. We gratefully acknowledge financial support from ANR under Grant No. 18-CE30-0005, from the Cell(n)Scale Labex (ANR-11-LABX-0038). V. Y. was partially supported by Institut Curie and cofinancing under PCOFUND-GA-2013-609102 grant. D.J.G.P. is funded and L.G. is partially supported by the Netherlands Organisation for Scientific Research (NWO/OCW), as part of the Vidi scheme and the Frontiers of Nanoscience program and by the ERC-CoG grant HexaTissue. The authors thank Dr. Philippe Chavrier, Institut Curie, for the HT1080 cells. V. Y. and P. S. initially designed the experiment. V. Y. and F. A. performed the experiments. D. J. G. P., C. B.-M., and L. G. developed the theory. D. J. G. P. performed the numerical simulations. V. Y., D. J. G. P., and C. B.-M. analyzed and interpreted the data. V. Y., D. J. G. P., C. B.-M., L. G., and P. S. wrote the manuscript.

APPENDIX: METHODS

1. Cell culture

HT1080 cells were cultured in Dulbecco's modified Eagle's medium (high glucose + GlutaMAX, Gibco) supplemented with 10% FBS (Sigma) and 1% antibiotics solution [penicillin (10 000 units/mL) + streptomycin (10 mg/mL), Gibco] at 37 °C, 5% CO₂, and 90% humidity.

2. Time-lapse microscopy

Time-lapse multifield experiments were performed in phase contrast on an automated inverted microscope (Olympus IX71) equipped with thermal and CO₂ regulations. Typical field of view (FOV) was 1.5×1.5 mm². The position of the measured sample and the acquisitions with a CCD camera (Retiga 4000R, QImaging) were controlled by METAMORPH (Universal Imaging) software. The typical delay between two successive images of the same field was set to 15 min.

3. Image processing

Stripes were cropped from the raw images using the ImageJ public domain software [62]. The orientation field was obtained by computing the local structure tensor with ImageJ plug-in OrientationJ [63] within windows of $23.75 \times 23.75 \mu\text{m}^2$. S corresponds to the anisotropy level, and the nematic director \mathbf{n} was computed from the output angle. The velocity field in the monolayer was mapped by particle image velocimetry analysis. Stacks of images were analyzed with a custom-made PIV algorithm based on the MatPIV [64,65] software package. The window size was set to 32 pixels = $23.75 \mu\text{m}$ with a 0.5 overlap. Visualization of the orientation field and velocity field were performed with PYTHON plotting library Matplotlib [66].

4. Micropatterning technique

Clean glass substrates were first uniformly coated with a cell-repellent layer (interpenetrated gel of acrylamide and polyethylene glycol). A photoresist mask was then structured directly on top of the layer by classical photolithography methods and air plasma was used to locally etch the protein-repellent coating through this mask. The photoresist was then removed with acetone yielding a cell-repellent substrate where bare glass domains on which cells can adhere have been defined [38,67].

5. Statistical analysis

Statistical analysis of HT1080 time-lapse data was performed with MATLAB. Experiments were performed in at least four replicas, each using six well plates with stripes of three distinct width ranges (for $L_x = 300\text{--}400$ and $400\text{--}600 \mu\text{m}$) or distinct widths (for $L_x = 700, 800, 1000 \mu\text{m}$) and plain glass slides. Monolayers reach confluency at least 12 h after cells were seeded. The profiles of velocity, $+1/2$ defect density, and polarization [Figs. 1(d), 3(a), and 3(c)] were averaged over a 25 h period starting after confluence. Error bars represent the standard deviations over all the FOVs averaged in time and along the channel length (y axis) (pooling all experiments for specific stripe width $\pm 5\%$). Following is the list of the stripes binned by widths $L_x \pm 5\%$ analyzed in the present study and the corresponding number N of FOVs used for the orientation field and PIV analysis cells: $[L_x (\mu\text{m}), N] = (300, 95), (400, 40), (500, 68), (600, 47), (700, 38), (800, 43), (1000, 29), (\text{boundary-free}, 24)$. Minimal distance between FOVs on same stripe exceeded 3 mm and no more than two FOVs were counted per stripe.

Statistical analysis of data from the numerical simulations was performed using a combination of C++ and PYTHON. For each parameter value, simulations were initialized with random, structureless director and velocity fields. Each simulation was run for 10^5 time steps before measurements were made, data were then collected over the following 10^6 time steps. We approximate the

hydrodynamic decorrelation time in the bulk to be of the order of 10^4 time steps; thus, measurements are taken over ~ 100 times the decorrelation time. To generate the velocity and density profiles across the width of the strip, data were first averaged over the length of the strip and in time. We assume the system is ergodic and measurements are taken over ~ 100 times the bulk hydrodynamic decorrelation time. Density and polarization fields for the topological defects were generated by further coarse graining the system in the x direction, which was done with a bin size of $L_x/50$. This scale is chosen to balance between forming an accurate estimate of the local density against the need to resolve features in the fields. All simulation error bars show the variation over time, thus exposing the intrinsic variability in the system. We estimate the standard error of the mean would have a variability reduced by a factor of ~ 10 estimated from the hydrodynamic decorrelation time.

6. Chirality of the edge flows

The direction of the edge flow was calculated as follows. For each field of view the difference between v_y values in $23 \mu\text{m}$ layer adjacent to the left and to the right boundaries was averaged along the stripe length and time, $\langle v_y(-L_x/2) - v_y(L_x/2) \rangle$, where L_x is the width of the stripe. The chirality of the edge flow [Fig. 1(f)] was defined as right for $\langle \cdot \rangle > std$, left for $\langle \cdot \rangle < -std$, and unclear for $|\langle \cdot \rangle| < std$.

7. Average fields around defects

In the following, we explain the calculation of the averaged velocity and averaged director fields over defect populations. $+1/2$ and $-1/2$ defect positions were detected by searching for the local minima of an order parameter in the window of $20 \times 20 \mu\text{m}^2$ in the orientation map obtained by the OrientationJ plug-in. $+1/2$ defects and their direction were determined using the procedure explained in Ref. [56]. For each detected defect, the velocity and director maps were aligned with respect to the corresponding defect direction and then cropped over a window of size $250 \times 250 \mu\text{m}^2$ centered at the defect core. Finally, we computed the ensemble averages over different sets of $+1/2$ defects to obtain the averaged fields. In the case of the averaged fields for random positions that are shown in Fig. S5 in Supplemental Material [39], the abovementioned procedure was the same except that the defect positions were replaced by random positions within the cell monolayer.

8. Numerical simulations

We numerically solve the hydrodynamic equations for the nematic tensor \mathbf{Q} and the flow velocity \mathbf{v} given by Eqs. (1) with active stress given by Eq. (3).

The system of equations is numerically integrated using a finite difference scheme on a rectangular grid of size $L_x \times L_y$, subject to periodic boundary conditions at

$y = \pm L_y/2$ and Navier boundary conditions, i.e., $\sigma \cdot N = -\xi v$, with N the boundary normal and ξ a drag coefficient, at $x = \pm L_x/2$. The aspect ratio of the channels was simulated at $L_y/L_x = 2$ and the resolution of the grid was $\Delta x = \Delta y = \epsilon$. To render Eqs. (1)–(3) dimensionless we rescale length by core radius ϵ , time by the nematic relaxational timescale $\tau_r = \gamma \epsilon^2/K$, and stress by elastic stress $\sigma = K/\epsilon^2$. All quantities plotted in Figs. 1, 3, and 4 are rescaled accordingly. In Fig. 5, where ϵ varies, the unit length was fixed to 0.1 in simulation units. In these units, we set $\lambda = 0.5$, $\eta = 30$, $\mu = 0.1$, $\xi = 0.01$, $\alpha = -10$, $\tau = 0, -2.5, -5.0, -7.5, -10$, and $L_x = 100, 200, 300, 400, 500$.

-
- [1] V. Hakim and P. Silberzan, *Collective Cell Migration: A Physics Perspective*, *Rep. Prog. Phys.* **80**, 076601 (2017).
- [2] B. Ladoux and R. M. Mège, *Mechanobiology of Collective Cell Behaviours*, *Nat. Rev. Mol. Cell Biol.* **18**, 743 (2017).
- [3] E. Scarpa and R. Mayor, *Collective Cell Migration in Development*, *J. Cell Biol.* **212**, 143 (2016).
- [4] M. Poujade, E. Grasland-Mongrain, A. Hertzog, J. Jouanneau, P. Chavrier, B. Ladoux, A. Buguin, and P. Silberzan, *Collective Migration of an Epithelial Monolayer in Response to a Model Wound*, *Proc. Natl. Acad. Sci. U.S.A.* **104**, 15988 (2007).
- [5] E. Ben-Jacob, I. Cohen, and D. L. Gutnick, *Cooperative Organization of Bacterial Colonies: From Genotype to Morphotype*, *Annu. Rev. Microbiol.* **52**, 779 (1998).
- [6] K. J. Cheung and A. J. Ewald, *A Collective Route to Metastasis: Seeding by Tumor Cell Clusters*, *Science* **352**, 167 (2016).
- [7] P. Friedl and D. Gilmour, *Collective Cell Migration in Morphogenesis, Regeneration and Cancer*, *Nat. Rev. Mol. Cell Biol.* **10**, 445 (2009).
- [8] X. Trepát and E. Sahai, *Mesoscale Physical Principles of Collective Cell Organization*, *Nat. Phys.* **14**, 671 (2018).
- [9] A. Doostmohammadi and B. Ladoux, *Physics of Liquid Crystals in Cell Biology*, *Trends Cell Biol.* **32**, 140 (2022).
- [10] T. E. Angelini, E. Hannezo, X. Trepát, M. Marquez, J. J. Fredberg, and D. A. Weitz, *Glass-like Dynamics of Collective Cell Migration*, *Proc. Natl. Acad. Sci. U.S.A.* **108**, 4714 (2011).
- [11] J. A. Park, J. H. Kim, D. Bi, J. A. Mitchel, N. T. Qazvini *et al.*, *Unjamming and Cell Shape in the Asthmatic Airway Epithelium*, *Nat. Mater.* **14**, 1040 (2015).
- [12] S. Garcia, E. Hannezo, J. Elgeti, J. F. Joanny, P. Silberzan, and N. S. Gov, *Physics of Active Jamming during Collective Cellular Motion in a Monolayer*, *Proc. Natl. Acad. Sci. U.S.A.* **112**, 15314 (2015).
- [13] L. Atia, D. Bi, Y. Sharma, J. A. Mitchel, B. Gweon *et al.*, *Geometric Constraints during Epithelial Jamming*, *Nat. Phys.* **14**, 613 (2018).
- [14] C. Blanch-Mercader, V. Yashunsky, S. Garcia, G. Duclos, L. Giomi, and P. Silberzan, *Turbulent Dynamics of Epithelial Cell Cultures*, *Phys. Rev. Lett.* **120**, 208101 (2018).
- [15] A. Palamidessi, C. Malinverno, E. Frittoli, S. Corallino, E. Barbieri *et al.*, *Unjamming Overcomes Kinetic and Proliferation Arrest in Terminally Differentiated Cells and Promotes Collective Motility of Carcinoma*, *Nat. Mater.* **18**, 1252 (2019).
- [16] S. J. Streichan, M. F. Lefebvre, N. Noll, E. F. Wieschaus, and B. I. Shraiman, *Global Morphogenetic Flow Is Accurately Predicted by the Spatial Distribution of Myosin Motors*, *eLife* **7**, e27454 (2018).
- [17] Y. Maroudas-Sacks, L. Garion, L. Shani-Zerbib, A. Livshits, E. Braun, and K. Keren, *Topological Defects in the Nematic Order of Actin Fibers as Organization Centers of Hydra Morphogenesis*, *Nat. Phys.* **17**, 251 (2021).
- [18] T. B. Saw, A. Doostmohammadi, V. Nier, L. Kocgozlu, S. Thampi, Y. Toyama, P. Marcq, C. T. Lim, J. M. Yeomans, and B. Ladoux, *Topological Defects in Epithelia Govern Cell Death and Extrusion*, *Nature (London)* **544**, 212 (2017).
- [19] L. Giomi, M. J. Bowick, X. Ma, and M. C. Marchetti, *Defect Annihilation and Proliferation in Active Nematics*, *Phys. Rev. Lett.* **110**, 228101 (2013).
- [20] L. Giomi, M. J. Bowick, P. Mishra, R. Sknepnek, and M. C. Marchetti, *Defect Dynamics in Active Nematics*, *Phil. Trans. R. Soc. A* **372**, 20130365 (2014).
- [21] G. Duclos, C. Erlenkämper, J. F. Joanny, and P. Silberzan, *Topological Defects in Confined Populations of Spindle-Shaped Cells*, *Nat. Phys.* **13**, 58 (2017).
- [22] S. P. Thampi, R. Golestanian, and J. M. Yeomans, *Instabilities and Topological Defects in Active Nematics*, *Europhys. Lett.* **105**, 18001 (2014).
- [23] L. Giomi, *Geometry and Topology of Turbulence in Active Nematics*, *Phys. Rev. X* **5**, 031003 (2015).
- [24] S. R. K. Vedula, M. C. Leong, T. L. Lai, P. Hersen, A. J. Kabla, C. T. Lim, and B. Ladoux, *Emerging Modes of Collective Cell Migration Induced by Geometrical Constraints*, *Proc. Natl. Acad. Sci. U.S.A.* **109**, 12974 (2012).
- [25] S. Z. Lin, W. Y. Zhang, D. Bi, B. Li, and X. Q. Feng, *Energetics of Mesoscale Cell Turbulence in Two-Dimensional Monolayers*, *Communications in Physics* **4**, 21 (2021).
- [26] L. Wan, K. Ronaldson, M. Park, G. Taylor, Y. Zhang, J. Gimble, and G. Vunjak-Novakovic, *Micropatterned Mammalian Cells Exhibit Phenotype-Specific Left-Right Asymmetry*, *Proc. Natl. Acad. Sci. U.S.A.* **108**, 12295 (2011).
- [27] Y. Tee, T. Shemesh, V. Thiagarajan, R. Hariadi, K. Anderson, C. Page, N. Volkmann, D. Hanein, S. Sivaramakrishnan, M. Kozlov *et al.*, *Cellular Chirality Arising from the Self-Organization of the Actin Cytoskeleton*, *Nat. Cell Biol.* **17**, 445 (2015).
- [28] S. Naganathan, S. Fürthauer, M. Nishikawa, F. Jülicher, and S. Grill, *Active Torque Generation by the Actomyosin Cell Cortex Drives Left-Right Symmetry Breaking*, *eLife* **3**, e04165 (2014).
- [29] A. Kumar, A. Maitra, M. Sumit, S. Ramaswamy, and G. Shivashankar, *Actomyosin Contractility Rotates the Cell Nucleus*, *Sci. Rep.* **4**, 1 (2014).
- [30] F. Segerer, F. Thüroff, A. Alberola, E. Frey, and J. Rädler, *Emergence and Persistence of Collective Cell Migration on Small Circular Micropatterns*, *Phys. Rev. Lett.* **114**, 228102 (2015).

- [31] A. Chin, K. Worley, P. Ray, G. Kaur, J. Fan, and L. Wan, *Epithelial Cell Chirality Revealed by Three-Dimensional Spontaneous Rotation*, *Proc. Natl. Acad. Sci. U.S.A.* **115**, 12188 (2018).
- [32] G. Duclos, C. Blanch-Mercader, V. Yashunsky, G. Salbreux, J. F. Joanny, J. Prost, and P. Silberzan, *Spontaneous Shear Flow in Confined Cellular Nematics*, *Nat. Phys.* **14**, 728 (2018).
- [33] Y. Tee, W. Goh, X. Yong, H. Ong, J. Hu, I. Tay, S. Shi, S. Jalal, S. Barnett, P. Kanchanawong *et al.*, *Actin Polymerization and Crosslinking Drive Left-Right Asymmetry in Single Cell and Cell Collectives*, *bioRxiv:2021.04.22.440942*.
- [34] H. Wioland, F. G. Woodhouse, J. Dunkel, J. O. Kessler, and R. E. Goldstein, *Confinement Stabilizes a Bacterial Suspension into a Spiral Vortex*, *Phys. Rev. Lett.* **110**, 268102 (2013).
- [35] E. Lushi, H. Wioland, and R. E. Goldstein, *Fluid Flows Created by Swimming Bacteria Drive Self-Organization in Confined Suspensions*, *Proc. Natl. Acad. Sci. U.S.A.* **111**, 9733 (2014).
- [36] H. Wioland, E. Lushi, and R. E. Goldstein, *Directed Collective Motion of Bacteria under Channel Confinement*, *J. Phys.* **18**, 075002 (2016).
- [37] K. Beppu, Z. Izri, T. Sato, Y. Yamanishi, Y. Sumino, and Y. T. Maeda, *Edge Current and Pairing Order Transition in Chiral Bacterial Vortices*, *Proc. Natl. Acad. Sci. U.S.A.* **118**, e2107461118 (2021).
- [38] G. Duclos, M. Deforet, H. G. Yevick, O. Cochet-Escartin, F. Ascione *et al.*, *Controlling Confinement and Topology to Study Collective Cell Behaviors*, *Methods in Molecular Biology* (Humana Press Inc., New York, NY, 2018), pp. 387–399, [10.1007/978-1-4939-7701-7_28](https://doi.org/10.1007/978-1-4939-7701-7_28).
- [39] See Supplemental Material at <http://link.aps.org/supplemental/10.1103/PhysRevX.12.041017> for additional information on the conditions that were used in theoretical framework, examples of contrast time-lapse of an HT1080 cell monolayers (Movies 1 and 2), and on the statistical analysis Figs. S1–S7.
- [40] M. C. Marchetti, J. F. Joanny, S. Ramaswamy, T. B. Liverpool, J. Prost, M. Rao, and R. Aditi Simha, *Hydrodynamics of Soft Active Matter*, *Rev. Mod. Phys.* **85**, 1143 (2013).
- [41] A. Doostmohammadi, J. Ignés-Mullol, J. M. Yeomans, and F. Sagués, *Active Nematics*, *Nat. Commun.* **9**, 1 (2018).
- [42] J. Dunkel, S. Heidenreich, K. Drescher, H. H. Wensink, M. Bär M, and R. E. Goldstein, *Fluid Dynamics of Bacterial Turbulence*, *Phys. Rev. Lett.* **110**, 228102 (2013).
- [43] A. Be'er, B. Ilkanaiv, R. Gross, D. B. Kearns, S. Heidenreich *et al.*, *A Phase Diagram for Bacterial Swarming*, *Communications in Physics* **3**, 66 (2020).
- [44] K. Copenhagen, R. Alert, N. S. Wingreen, and J. W. Shaevitz, *Topological Defects Induce Layer Formation in Myxococcus xanthus Colonies*, *arXiv:200103804*.
- [45] Z. You, D. J. Pearce, A. Sengupta, and L. Giomi, *Geometry and Mechanics of Microdomains in Growing Bacterial Colonies*, *Phys. Rev. X* **8**, 031065 (2018).
- [46] P. Lee and C. W. Wolgemuth, *Crawling Cells Can Close Wounds without Purse Strings or Signaling*, *PLoS Comput. Biol.* **7**, e1002007 (2011).
- [47] O. Cochet-Escartin, J. Ranft, P. Silberzan, and P. Marcq, *Border Forces and Friction Control Epithelial Closure Dynamics*, *Biophys. J.* **106**, 65 (2014).
- [48] S. Banerjee, K. J. Utuje, and M. C. Marchetti, *Propagating Stress Waves during Epithelial Expansion*, *Phys. Rev. Lett.* **114**, 228101 (2015).
- [49] C. Blanch-Mercader, R. Vincent, E. Bazellières, X. Serra-Picamal, X. Trepas, and J. Casademunt, *Effective Viscosity and Dynamics of Spreading Epithelia: A Solvable Model*, *Soft Matter* **13**, 1235 (2017).
- [50] S. Tili, E. Gauquelin, B. Li, O. Cardoso, B. Ladoux *et al.*, *Collective Cell Migration without Proliferation: Density Determines Cell Velocity and Wave Velocity*, *R. Soc. Open Sci.* **5**, 172421 (2018).
- [51] P. Recho, J. Fouchard, T. Wyatt, N. Khalilgharibi, G. Charras, and A. Kabla, *Tug-of-War between Stretching and Bending in Living Cell Sheets*, *Phys. Rev. E* **102**, 012401 (2020).
- [52] T. J. Pedley and J. O. Kessler, *Hydrodynamic Phenomena in Suspensions of Swimming Microorganisms*, *Annu. Rev. Fluid Mech.* **24**, 313 (1992).
- [53] R. Aditi Simha and S. Ramaswamy, *Hydrodynamic Fluctuations and Instabilities in Ordered Suspensions of Self-Propelled Particles*, *Phys. Rev. Lett.* **89**, 058101 (2002).
- [54] S. Naganathan, T. Middelkoop, S. Fürthauer, and S. Grill, *Actomyosin-Driven Left-Right Asymmetry: From Molecular Torques to Chiral Self Organization*, *Curr. Opin. Cell Biol.* **38**, 24 (2016).
- [55] L. A. Hoffmann, K. Schakenraad, R. M. Merks, and L. Giomi, *Chiral Stresses in Nematic Cell Monolayers*, *Soft Matter* **16**, 764 (2020).
- [56] A. J. Vromans and L. Giomi, *Orientational Properties of Nematic Disclinations*, *Soft Matter* **12**, 6490 (2016).
- [57] G. Duclos, S. Garcia, H. Yevick, and P. Silberzan, *Perfect Nematic Order in Confined Monolayers of Spindle-Shaped Cells*, *Soft Matter* **10**, 2346 (2014).
- [58] M. Schwartz, R. Rogers, S. Singh, J. Lee, S. Loveland, J. Koepsel, E. Witze, S. Montanez-Sauri, K. Sung, E. Tokuda *et al.*, *A Quantitative Comparison of Human HT-1080 Fibrosarcoma Cells and Primary Human Dermal Fibroblasts Identifies a 3D Migration Mechanism with Properties Unique to the Transformed Phenotype*, *PLoS One* **8**, e81689 (2013).
- [59] L. Yamauchi, T. Hayata, M. Uwamichi, T. Ozawa, and K. Kawaguchi, *Chirality-Driven Edge Flow and Non-Hermitian Topology in Active Nematic Cells*, *arXiv:2008.10852*.
- [60] K. Kawaguchi, R. Kageyama, and M. Sano, *Topological Defects Control Collective Dynamics in Neural Progenitor Cell Cultures*, *Nature (London)* **545**, 327 (2017).
- [61] P. Guillamat, C. Blanch-Mercader, G. Pernollet, K. Kruse, and A. Roux, *Integer Topological Defects Organize Stresses Driving Tissue Morphogenesis*, *Nat. Mater.* **21**, 588 (2022).
- [62] T. Ferreira and W. Rasband, *ImageJ User Guide—IJ 1.46r*, <https://imagej.nih.gov/ij/docs/guide/>.
- [63] R. Rezakhaniha, A. Agianniotis, J. T. C. Schrauwen, A. Griffo, D. Sage, C. V. C. Bouten, F. N. van de Vosse, M. Unser, and N. Stergiopulos, *Experimental Investigation*

- of Collagen Waviness and Orientation in the Arterial Adventitia Using Confocal Laser Scanning Microscopy*, *Biomech. Model. Mechanobiol.* **11**, 461 (2012).
- [64] J. K. Sveen, *An Introduction to MatPIV v. 1.6.1* (University of Oslo, Oslo, 2004), <http://urn.nb.no/URN:NBN:no-27806>.
- [65] L. Petitjean, M. Reffay, E. Grasland-Mongrain, M. Poujade, B. Ladoux, A. Buguin, and P. Silberzan, *Velocity Fields in a Collectively Migrating Epithelium*, *Biophys. J.* **98**, 1790 (2010).
- [66] J. D. Hunter, *Matplotlib: A 2D Graphics Environment*, *Comput. Sci. Eng.* **9**, 90 (2007).
- [67] M. Deforet, V. Hakim, H. Yevick, G. Duclos, and P. Silberzan, *Emergence of Collective Modes and Tri-Dimensional Structures from Epithelial Confinement*, *Nat. Commun.* **5**, 3747 (2014).